Breast tomosynthesis imaging configuration optimization based on computer simulation

Shiyu Xu,[a] Linlin Cong,[b] Jianping Lu,[c,d] Otto Zhou,[c,d] Yueh Z. Lee,[e] and Ying Chen[a,b,*]
[a]Southern Illinois University, Department of Electrical and Computer Engineering, Carbondale, Illinois 62901
[b]Southern Illinois University, Biomedical Engineering Graduate Program, Carbondale, Illinois 62901
[c]The University of North Carolina, Department of Physics and Astronomy, and Curriculum in Applied Sciences and Engineering, Chapel Hill, North Carolina 27599
[d]The University of North Carolina, Lineberger Comprehensive Cancer Center, Chapel Hill, North Carolina 27599
[e]The University of North Carolina, Department of Radiology, Chapel Hill, North Carolina 27599

Abstract. Digital tomosynthesis is an innovative imaging technology for early breast cancer detection by providing three-dimensional anatomical information with fast image acquisition and low-dose radiation. Most of current breast tomosynthesis systems utilize a design where a single x-ray tube moves along an arc above objects over a certain angular range. The mechanical movement and patient motion during the scan may degrade image quality. With a carbon nanotube–based multibeam x-ray source, a new breast tomosynthesis modality is innovated, which will potentially produce better image quality with stationary beam sources and faster scan and it enables a variety of beam distributions. In this study, several beam distributions, such as beam sources spanning along a one-dimensional (1-D) parallel configuration and sources over a two-dimensional (2-D) rectangle shape are investigated based on computer simulations. Preliminary results show that 2-D rectangle shapes outperform 1-D parallel shapes by providing better Z-resolution, enhanced image contrast, reduced out-of-plane blur and artifacts and lower reconstruction noise. These benefits may expand tomosynthesis applications to diagnostic and interventional procedures. © 2014 SPIE and IS&T [DOI: 10.1117/1.JEI.23.1.013017]

Keywords: image acquisition; image quality; maximum likelihood with expectation maximization; modulation transfer function; spatial resolution; tomosynthesis; simulation.

Paper 13075 received Feb. 19, 2013; revised manuscript received Sep. 22, 2013; accepted for publication Jan. 2, 2014; published online Feb. 6, 2014.

1 Introduction

Digital tomosynthesis[1,2] is a three-dimensional (3-D) imaging modality with low dose radiation. It is a form of limited angle tomography that produces section images synthesized from a series of acquired projection images as the x-ray tube moves along a prescribed path. The typical total angular range of breast tomosynthesis imaging is <50 deg, and the number of projection images is limited to under 49 for a low dose radiation. Because the sampling is highly incomplete, the depth resolution is limited. Therefore, tomosynthesis does not produce the isotropic spatial resolution achievable with computed tomography (CT). However, due to the usage of cone-beam x-ray and flat panel detector, the resolution of a transversely reconstructed plane is often superior to CT.[1]

Tomosynthes has been applied to a wide variety of clinical applications over the years, which includes dental imaging, angiography, and imaging of the chest, bones, and breast. Digital breast tomosynthes (DBT)[1–4] is a very important application to improve early cancer detection. Conventional x-ray mammography is a two-dimensional (2-D) imaging modality, where overlapping tissue can hide objects of interest. Compared to mammography, the DBT can reduce the tissue superimposition and report accurate locations of lesions by applying a comparable dose level. Additionally, tomosynthesis system should support the potentials to perform tomosynthesis-guided interventional procedure[5] due to the ability to uncover lesions, the quick image acquisition, and the ease of use in conjunction with conventional radiography.

A typical tomosynthesis system is composed of an image acquisition system, image reconstruction, processing hardware/software suits and display terminals. Figure 1 shows a brief demonstration of a typical iso-centric DBT acquisition system, in which x-ray source moves along an arc path. For an optimal tomosynthesis imaging configuration, several factors must be optimized, such as scan time, scan angle, number of projections, spatial resolution, reconstructed slice thickness, and dose distribution. In the literature,[6] the effects of these factors on the detection of microcalcifications in the DBT were studied with 60 deg angular coverage in an arc configuration. The literature[7,8] did a similar job based on objective image quality criterions. The literature[9,10] estimated the number of projections and their total angular span to find the optimal configuration, which produces the optimal performance according to a task model clinical decision.

The limitations of current tomosynthesis systems include a longer scanning time than a conventional digital x-ray modality and a low spatial resolution. Both are resulted from the limitations of the current x-ray tube technology where a single x-ray tube is mounted on a rotating gantry and moves along an arc above objects over a certain angular range. Projection blur due to the source movement and patient motion is a major factor degrading the spatial resolution in image domain. For a continuous tube motion

X ray tube

Rotation Arc

Compression board
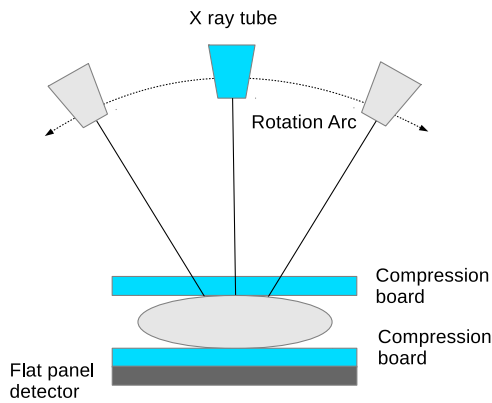
Compression board

Flat panel detector

Fig. 1 A demonstration of a typical digital breast tomosynthesis prototype system.

design, the higher the scanning speed, the larger the distance the x-ray tube travels during a fixed exposure time and the worse the x-ray focal spot blurs. In addition, longer time scanning will increase the probability of patient motion. The amount of blur which can be tolerated limits the scanning speed and angular coverage.

To conquer the limitations, literatures[11,12] proposed the concept of stationary digital breast tomosynthesis (s-DBT) using a carbon nanotube (CNT)–based x-ray source array. Instead of mechanically moving a single x-ray tube, the s-DBT applies a stationary x-ray source array, which generates x-ray radiation from different view angles by electronically activating the individual source prepositioned at the corresponding view angle, therefore eliminating the focal spot motion blurring from sources. The scanning speed is determined only by the detector readout time and the number of sources regardless of the angular coverage spans, such that the blur from patient motion can be reduced due to the quick scan. More importantly, the spatial-distributed multibeam x-ray sources also enable potentials to improve image qualities by wide varieties of flexible source distributions, which are not limited to a one-dimensional (1-D) configuration such as an arc or a parallel.

The purpose of this research is to investigate the potential benefits of more flexible distributions of beam sources. For this purpose, several spatial distributions, such as beam sources spanning along a 1-D line and sources over a 2-D plane parallel to the detector surface are studied with computer simulations. Impulse signal and wire signal cross a focus plane are simulated with these source distributions. Noise simulation is also performed. The simulated tomosynthesis datasets are reconstructed by maximum likelihood with expectation maximization (ML-EM) method. Resolution and noise properties are evaluated and compared through image quality criterion and human vision.

2 Materials and Methods

2.1 Simulated Tomosynthesis Datasets with Spatially Distributed Multibeam X-ray Tubes

In the s-DBT prototype,[12] multiple x-ray beams are positioned along a straight line parallel to the detector surface. The source is designed to have 25 x-ray beams spanning a distance of 570 mm from end to end. The linear spacing

between the x-ray beams varies to provide an even 2 deg angular coverage. Data source to object distance is kept as 640 mm. In addition, a flat panel detector is used for imaging acquisition. With a 0.14-mm detector pitch, the total projection size is 2048×1664. The literature[13] studies the effect of the key geometric factors on image quality with the s-DBT system.

In our simulation, two types of beam distributions are established. One is a 1-D parallel shape, which is similar with the straight line parallel configuration presented in literature.[12] The other is a 2-D rectangle shape. For each shape, various density distributions of beam sources are presented. To accelerate the simulations and reconstructions, we applied a 512×512 detector array with the pitch of 0.56 mm by rebinning the detector in the literature.[12] A simplified geometric configuration is applied as well. A slightly wider source-spanning distance is used to provide a larger angular coverage.

2.1.1 Beam sources with a uniform parallel shape

Figure 2 shows the brief profile for a tomosynthesis system with a uniform parallel shape of beam sources (UniformParal). UniformParal has 25 x-ray sources fixed on the x-axis. The total angle approximately covers 50 deg. Source to image distance (SID) is the vertical distance from x-ray sources to the detector, which is 692.8 mm. Beam sources in UniformParal are distributed uniformly from -323.06 to 323.06 mm along the x-axis. Space between two neighbors of x-ray tube is 26.9 mm. During each complete scan, the x-ray tube will be activated from left to the right one by one.

2.1.2 Beam sources with a nonuniform parallel shape with dense center

Two kinds of tomosynthesis systems with nonuniform parallel are established. One is shown in Fig. 3. Compared to Fig. 2, most of the parameters, including SID, total view angle, number of x-ray sources, and the range of the source span, are identical with those of UniformParal, however, the space between each pair is not equal. The closer the x-ray sources are assembled to the y-axis, the denser the sources are distributed, which is called nonuniform parallel shape distributed by dense center (ParalDC). Supposing the
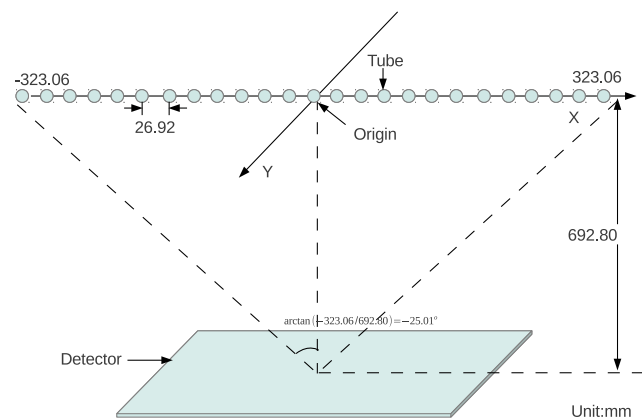
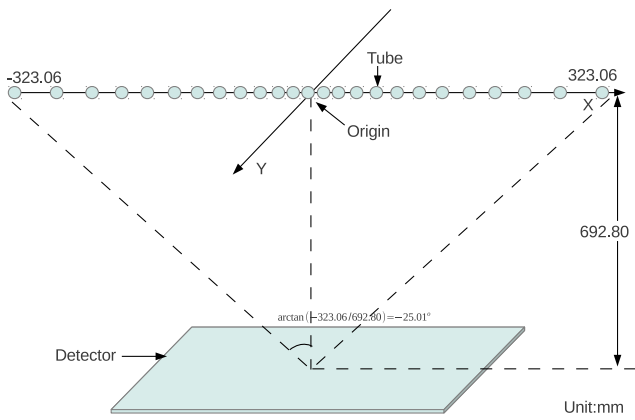**Fig. 2** The tomosynthesis system with a uniform parallel shape of beam sources.

Fig. 3 The tomosynthesis system with a nonuniform parallel shape of beam sources distributed by dense center.

smallest distance between two adjacent x-ray tubes is D, the spaces between two neighboring x-ray sources will be 1.2^7D, 1.2^6D, 1.2^5D, 1.2^4D, 1.2^3D, 1.2^2D, $1.2D$, D, D, D, D, D, D, $1.2D$, 1.2^2D, 1.2^3D, 1.2^4D, 1.2^5D, 1.2^6D, 1.2^7D from left to right. The value of D is 11.56 mm.

2.1.3 Beam sources with a nonuniform parallel shape with sparse center

The other nonuniform distribution for the parallel shape is shown in Fig. 4, which presents the parallel shape distributed with sparse center (ParalSC). Source beams turn to be sparse when they get closer to the *y*-axis. In the ParalSC configuration, except for spaces between x-ray sources, other parameters are kept the same. Given the smallest distance between two adjacent x-ray tubes is D, beam sources are placed with the distances from left to right being D, D, D, $1.2D$, 1.2^2D, 1.2^3D, 1.2^4D, 1.2^5D, 1.2^6D, 1.2^7D, 1.2^7D, 1.2^6D, 1.2^5D, 1.2^4D, 1.2^3D, 1.2^2D, $1.2D$, D, D, D. During each complete scan, the x-ray tube will be activated from left to the right one by one.

2.1.4 Beam sources with a uniform rectangle

The 2-D rectangle shapes of multibeam sources are emphasized in the following discussions. In the configuration,
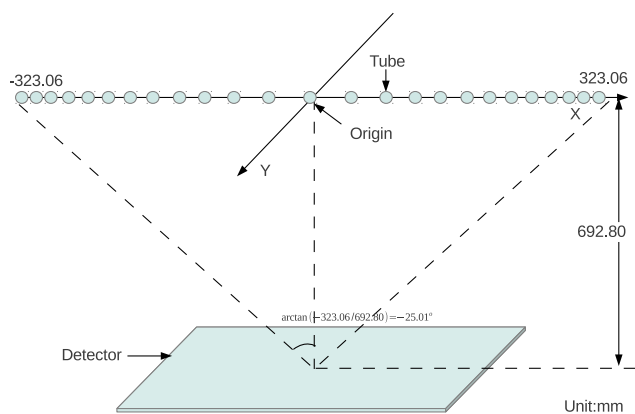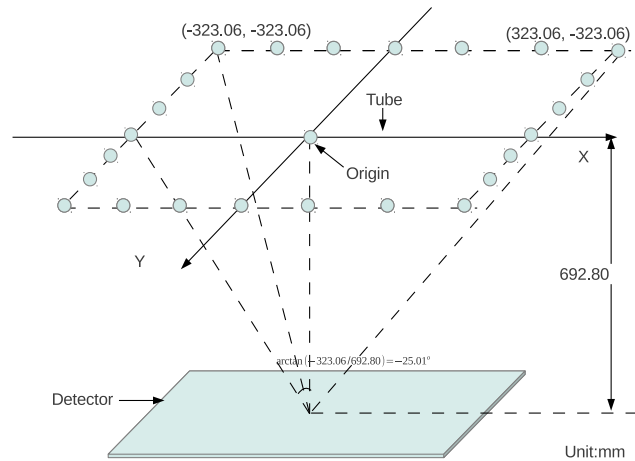

Fig. 5 The tomosynthesis system with a uniform rectangle shape of beam sources.

projection number, total angular coverage, and SID will stay the same as those of the parallel shapes. Figure 5 presents the configuration of uniform rectangle shape (UniformRec). Twenty four x-ray sources are fixed on a rectangle path. The rectangle is centered at origin with four vertexes being $(-323.06, -323.06)$, $(323.06, -323.06)$, $(323.06, 323.06)$, and $(-323.06, 323.06)$. The spaces between two neighbors of x-ray sources are uniform with a fixed value of 107.69 mm. The 25th x-ray is located at the origin. In a whole scan, the 24 x-ray sources will be triggered and started from the vertex $(-323.06, -323.06)$ one by one, and the x-ray located at the origin will be activated at last.

2.1.5 Beam sources with a nonuniform rectangle shape with dense near axes

Two kinds of nonuniform-distributed rectangle shape of beam sources are presented. Projection number, total angular coverage, SID and the four vertexes of rectangle configurations will stay unchanged to UnifromRec. But the density distributions of tubes vary. Figure 6 shows nonuniform

Fig. 4 The tomosynthesis system with a nonuniform parallel shape of beam sources distributed by sparse center.
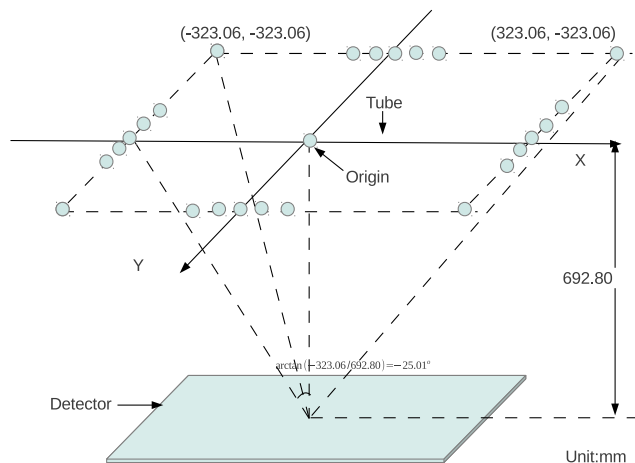

Fig. 6 The tomosynthesis system with a nonuniform rectangle shape of beam sources distributed by a dense near axis.

rectangle shape distributed by dense near axis (RecDNA), where density distribution of tubes is denser near to both axes and sparser far away from them. Given the smallest distance between two neighboring sources as D with the value of 53.84 mm, the spaces between two neighbors of x-ray sources on each side of the rectangle keep the pace of 3D, 2D, D, D, 2D, 3D from end to end. In a whole scan, 24 x-ray sources will be triggered starting from the vertex (−323.06, −323.06) one by one, and the x-ray located at the origin will be activated at last.

2.1.6 *Beam sources with a nonuniform rectangle shape with sparse near axes*

The other nonuniform rectangle shape is shown in Fig. 7, which is a nonuniform rectangle shape distributed by sparse near axis (RecSNA). In contrast to RecDNA, the beam sources tend to be sparse when they are approaching the axes (both X or Y). The smallest distance between two neighboring x-ray sources is D with the value of 53.84 mm. The spaces between two neighbors of x-ray sources on each side of the rectangle follow the pace of D, 2D, 3D, 3D, 2D, D from end to end. In a whole scan, the 24 x-ray sources will be triggered starting from the vertex (−323.06, −323.06) one by one, and the x-ray located at the origin will be activated at last.

2.2 *Signal Simulation and Measurement*

To compare the resolution property of these configurations, impulse signal[3] and wire signal[14] are simulated to generate projections by applying pixel driven ray-tracing method with each configuration. In the simulation, a partial pixel interpolation is performed when the forward projection falls into a noninteger pixel location. Reconstructed results from these simulated projections are compared along three axes. Line profiles and modulation transfer functions (MTFs) are evaluated for spatial resolution comparisons. Noise simulation is performed as well by adding Poisson noise on projections with an object-free scan. Through assessing standard deviations over reconstructed planes, noise properties for each source configuration can be measured.
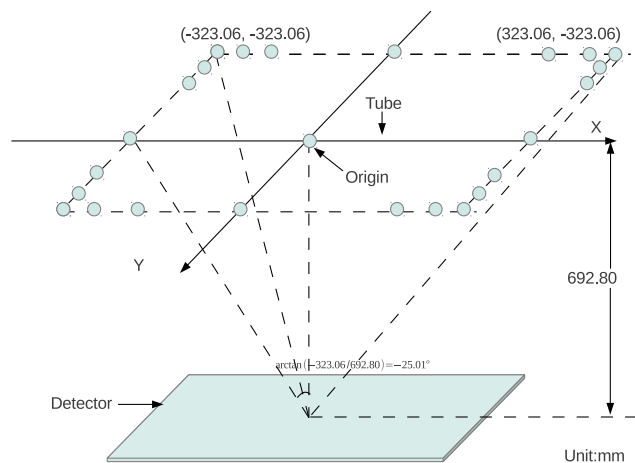
An impulse simulation is implemented with a single impulse signal shown in Fig. 8 to demonstrate the visibility and resolution property for each configuration. In addition, nine impulse signals are also simulated as shown in Fig. 9 to measure the average MTF on a focus plane, each of the signals is placed at the center of a grid and all the grids divide the focus plane into nine equal squares. Moreover, noise-free wire signal running horizontally (constant x) through the image space is also simulated. As shown in Fig. 10, the upper end of the wire is located at (0, −100, 652.80) and lower end is located at (0, 100, 672.80). The wire passes through the focus plane at the height of 30 mm away from the detector. Projection data are collected with the given beam sources and the wire signal. Spread functions cross different axes are measured on the reconstructed focus images.

2.3 *ML-EM Reconstruction Method*

Due to the highly incomplete sampling rate of tomosynthesis system, iterative-based methods, such as simultaneous algebraic reconstruction technique (SART)[15,16] and ML-EM[17,18] are usually superior[19] to Shannon–Nyquist-based method such as filtered back projection.[20] However, the SART and the ML-EM may lead to over-fitting to the noisy data.
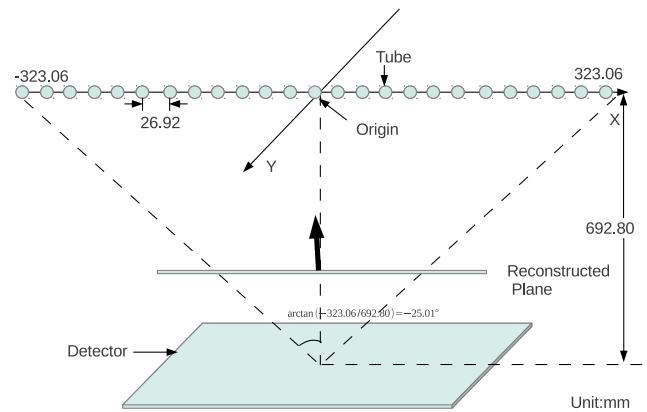

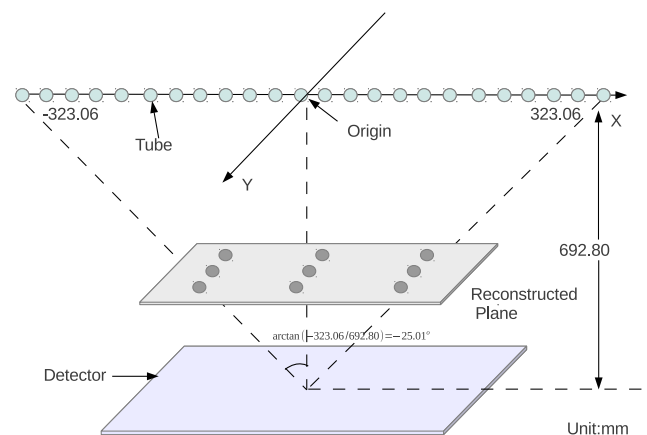**Fig. 8** An impulse signal located on a focus plane at 30 mm away from the detector.

Fig. 7 The tomosynthesis system with a nonuniform rectangle shape of beam sources distributed by sparse near axis.

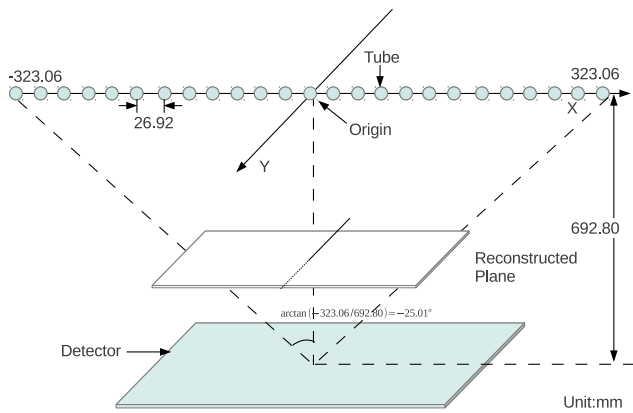**Fig. 9** Nine impulse signals located on a focus plane at 30 mm away from the detector.

Fig. 10 A wire signal crosses the focus plane with the upper end point (0, −100, 692.80-40) and the lower end point (0, 100, 692.80-20).

Penalized weighted least squares, penalized likelihood (PL), and precomputed BP-based PL method are strongly proposed in literature.[21–26]

In our investigations, the ML-EM is applied due to its implemental flexibility for various geometric configurations. In the classical model of x-ray imaging, the Poisson distribution of incident photon number dominates the physical process. Although x-ray detectors are not quanta counters, Poisson distribution still matches the signal statistics of mono-energetic x-ray detection.[27–29] The probability of photon number detected along the i-th X-ray is described mathematically as

$$P(Y_i = y_i) = \frac{\theta_i^{y_i} e^{-\theta_i}}{y_i!},$$

where Y_i is a random variable counting the observed photons on the detector along i'th x-ray beam; y_i is the observation of Y_i; θ_i is the expectation value of the random variable Y_i. In the classical physical model, θ_i can be expressed as

$$\theta_i = d_i e^{-\langle u, l_i \rangle},$$

where d_i is the intensity of the incident x-ray beam; u is a linear attenuation coefficient vector to be estimated, each component of which is roughly to be equated with the density of a voxel and the l_i denotes the vector of the intersection length between the i'th x-ray and each voxel. The negative log-likelihood function of all observed photons on the detector can be written as:

$$L(u) = \sum_i^M \{d_i e^{-\langle u, l_i \rangle} + y_i \langle u, l_i \rangle\} + c,$$

by the assumption that $\{Y_i\}_{i \in [1,M]}$ are independent and identically distributed, where c is constant and M is the number of x-ray. Through maximizing the objective function, optimal u can be estimated.
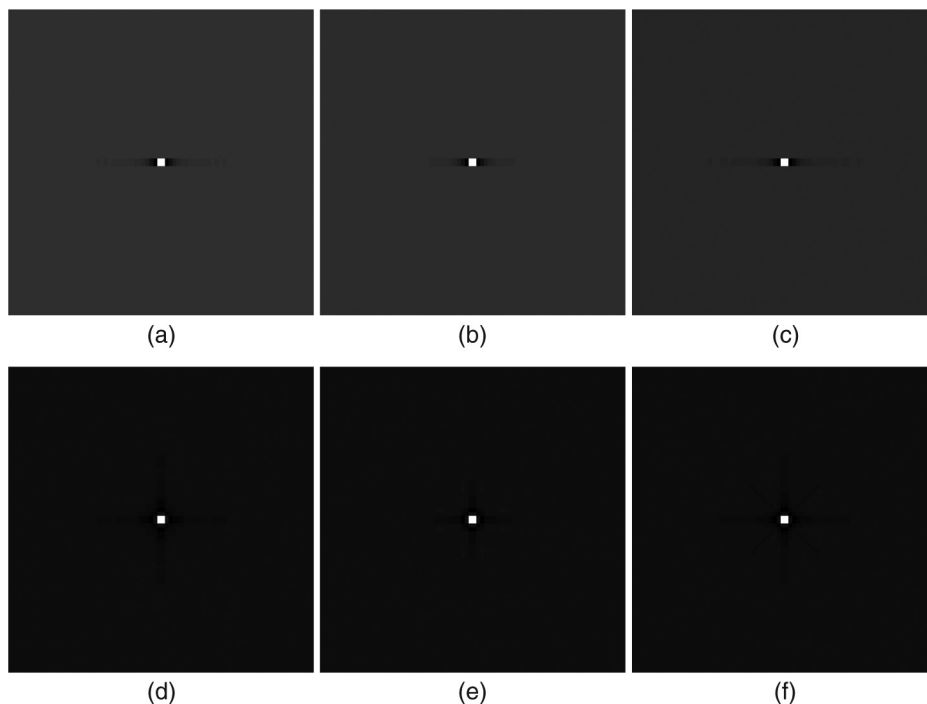

Fig. 11 The reconstructed results of impulse signal on the focus plane for the given beam source configurations. (a) The reconstructed result of impulse signal on the focus plane for UniformParal: Lower contrast and obvious artifacts along the scan direction; (b) the reconstructed result of impulse signal on the focus plane for ParalDC: Lower contrast and obvious artifacts along the scan direction; (c) the reconstructed result of impulse signal on the focus plane for ParalSC: Lower contrast and obvious artifacts along the scan direction; (d) the reconstructed result of impulse signal on the focus plane for UniformRec: higher contrast and less obvious artifacts; (e) the reconstructed result of impulse signal on the focus plane for RecDNA: higher contrast and less obvious artifacts; (f) The reconstructed result of impulse signal on the focus plane for RecSNA: higher contrast and less obvious artifacts.
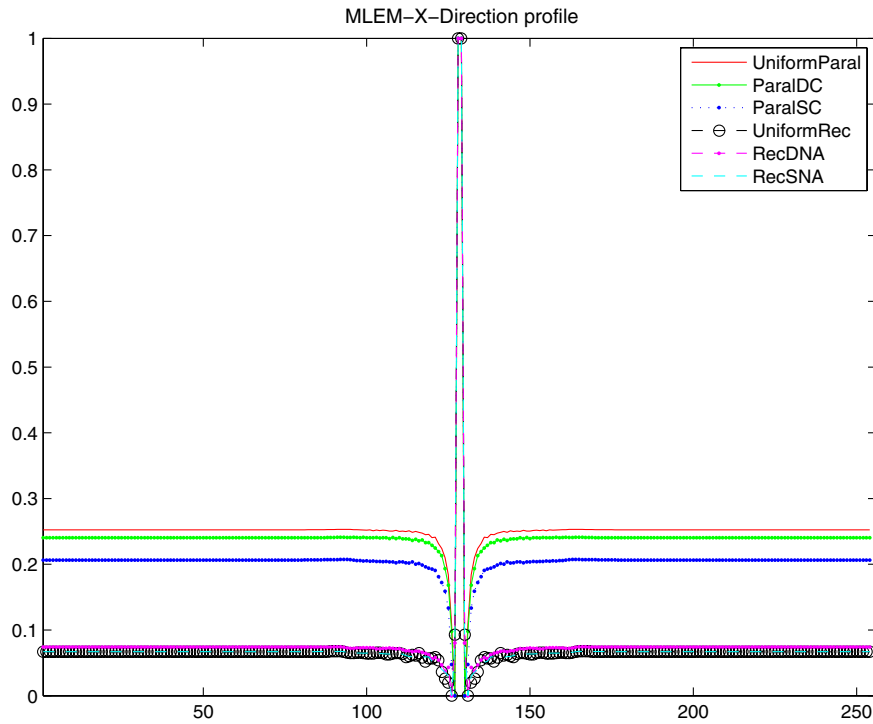
Fig. 12 Line profiles along the X direction crossing the impulse responses.

In general, to solve the optimization directly is intractable. But by EM method, a series of surrogate functions are constructed. The optimal estimation of u for $L(u)$ can be approached monotonically by optimal solutions of surrogate function $Q(u|u^{(n)})$, each of which is bounded by $L(u)$ and equal with $L(u)$ at u^n.

There are two steps in each iteration of the EM algorithm: In the E-step, the "complete data" are estimated by calculating their expectation, given the "incomplete data" y and the current solution u^n. In the M-step, the likelihood function of the "complete data" is maximized, assuming the estimated "complete data" from the E-step are correct.
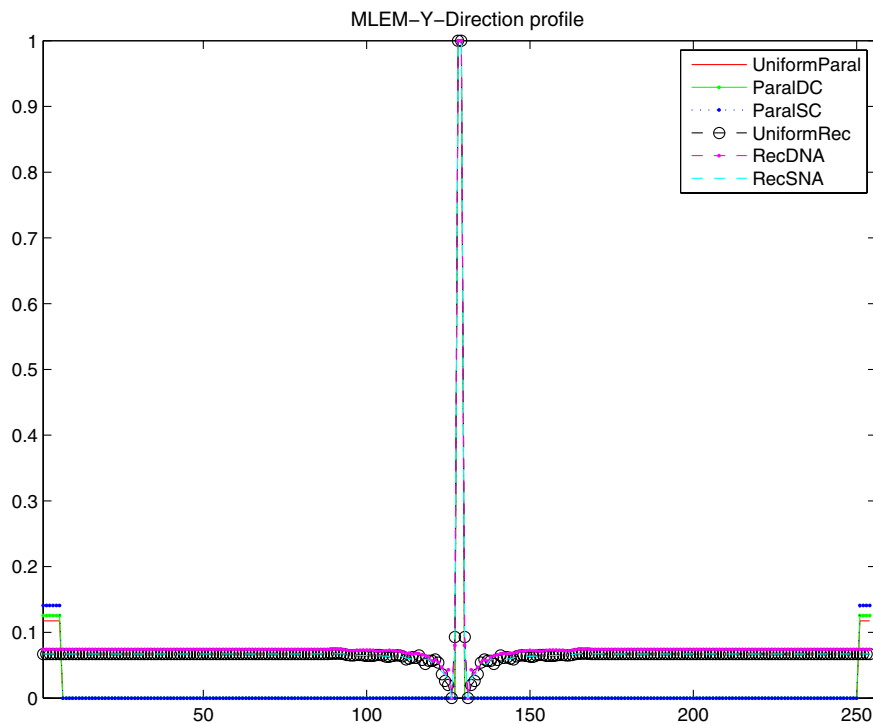

Fig. 13 Profiles along the Y direction crossing the impulse responses.
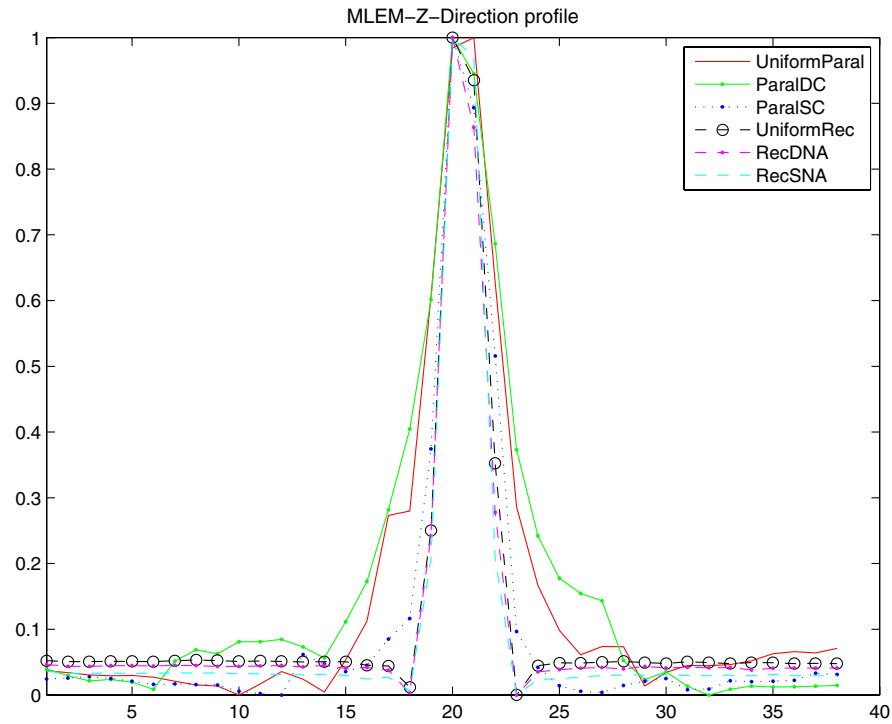
Fig. 14 Line profiles along the *Z* direction crossing the impulse responses.

The log-likelihood function based on expectation of "complete data" is represented by the function $Q(u|u^{(n)})$,

E-step: compute $Q(u|u^{(n)})$ using y and $u^{(n)}$

M-step: find $u^{(n+1)} = \arg\max\{Q(u|u^{(n)})\}$.

The iterative solution is given as below:

$$u_j^{(n+1)} = u_j^n + \frac{u_j^n \sum_i l_{i,j}(d_i e^{-\langle u^n, l_i\rangle} - y_i)}{\sum_i (l_{i,j}\langle l_i, u^{(n)}\rangle d_i e^{-\langle u^n, l_i\rangle}}.$$
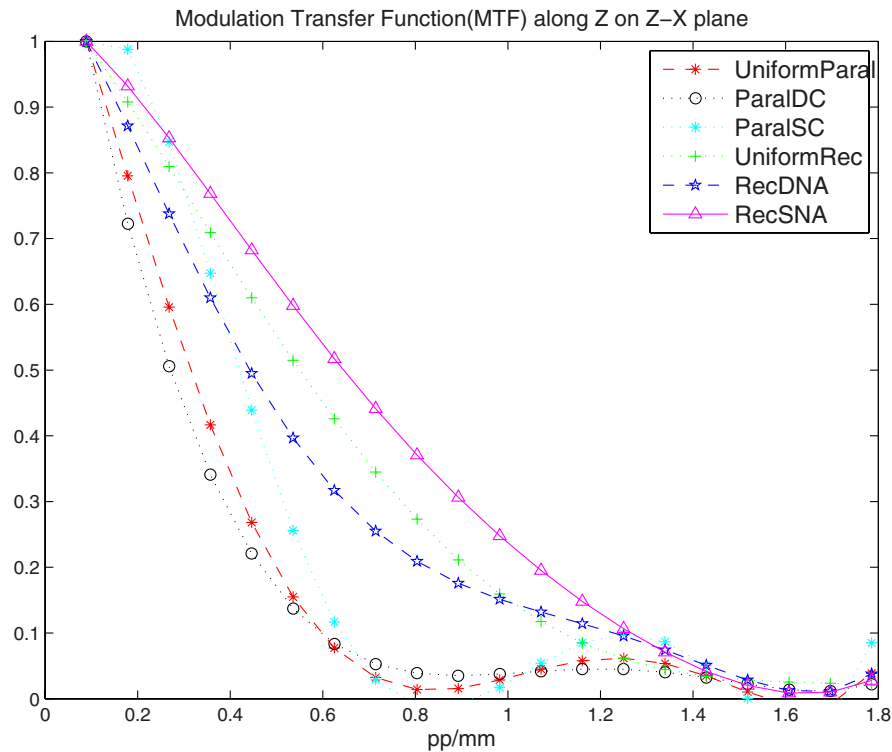

Fig. 15 Modulation transfer function (MTF) along the *Z* direction on the *Z*–*X* plane crossing the impulse responses.
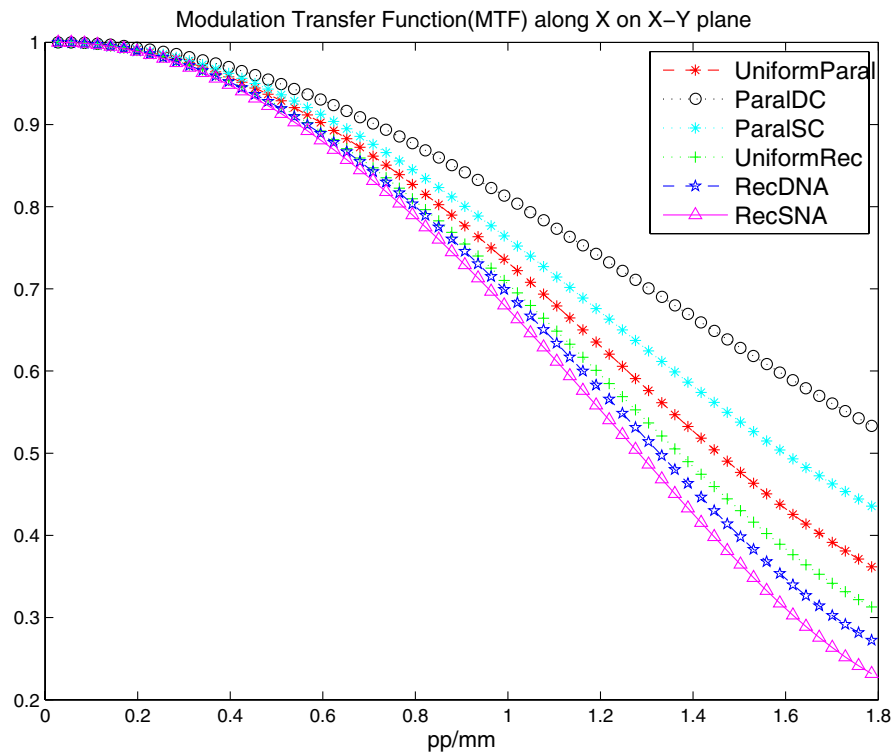
Fig. 16 The MTF along the *X* direction on the *X*–Y plane crossing the impulse responses.

The ML-EM iterative procedure is applied on each dataset obtained from different configurations and signals with 10 iterations.

3 Experiments and Results

3.1 *Impulse Response of the Six Beam Source Configurations in the Tomosynthesis System*

Figures 11(a)–11(f) show reconstructed results of a impulse signal on the focus plane with the six beam configurations. These results demonstrate that all configurations have the ability to produce 3-D results. The image contrast between the object and background with the rectangle shape is slightly higher than the one with parallel shape. Although

the artifacts along the scanning orientation exist within the rectangle configurations, they are less obvious than those within the parallel configurations.

Figure 12 draws the line profiles of the impulse responses shown above along the *x*-axis on the *X*–Y plane. The figure confirms that rectangle configurations produce better contrast and fewer artifacts along the object. For the same shape, there is no obvious difference among various distributions of density.

Figure 13 reports the line profiles along the *Y*-direction crossing the signals. Due to the absence of sources along this direction, there is no obvious artifact in parallel configurations which also produce a sharper edge along the direction. That conforms to the conclusion in literature,[5–8] which
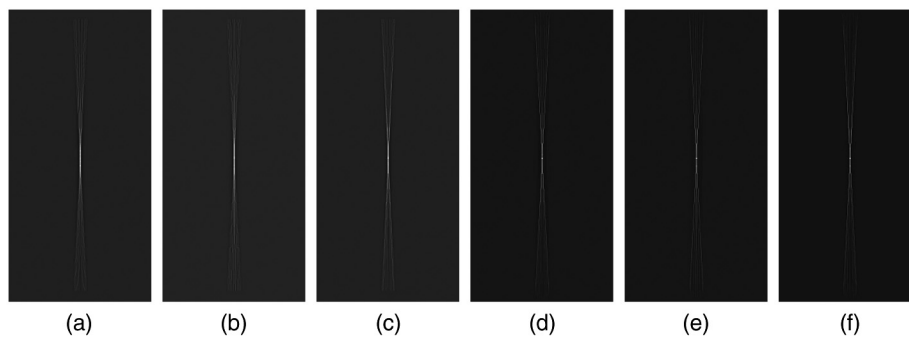

Fig. 17 The reconstructed results of wire signal on the focus plane for the given image acquisition configurations. (a) The reconstructed result of wire signal on the focus plane for UniformPara: more out-of-plane texture; (b) the reconstructed result of wire signal on the focus plane for ParalDC: more out-of-plane texture; (c) the reconstructed result of wire signal on the focus plane for ParalSC: more out-of-plane texture; (d) the reconstructed result of wire signal on the focus plane for UniformRec: sharper edge and less out-of-plane texture; (e) the reconstructed result of wire signal on the focus plane for RecDNA: sharper edge and less out-of-plane texture; (f) the reconstructed result of wire signal on the focus plane for RecSNA: sharper edge and less out-of-plane texture.
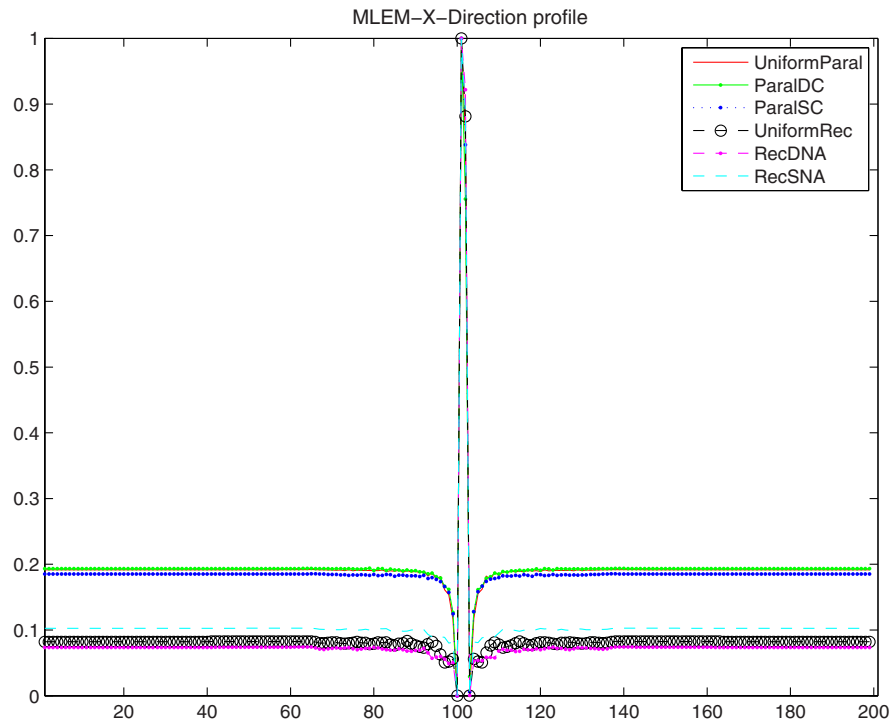
Fig. 18 Line profiles along the *X* direction crossing the wire responses.

say a narrow angular coverage can enhance the boundary of microcalcification. However, 3-D information may be lost as a result of the absent samplings.

Figure 14 shows the line profiles in the *Z*-direction along the signals. The impulse responses with rectangle shapes are much sharper than those from parallel shapes. For parallel configurations, the depth resolution of uniform configuration is worse than that of ParalSC but better than that of ParalDC. As to the rectangle configurations, the RecSNA provides a slightly better depth resolution than the other two. Both UniformRec and RecDNA yield similar results to each other.

To further quantify the z-resolution improvement for rectangle shapes, the MTFs of the impulse response, shown in Fig. 15, are evaluated in the *Z*-direction on the *Z*–*X* plane. At
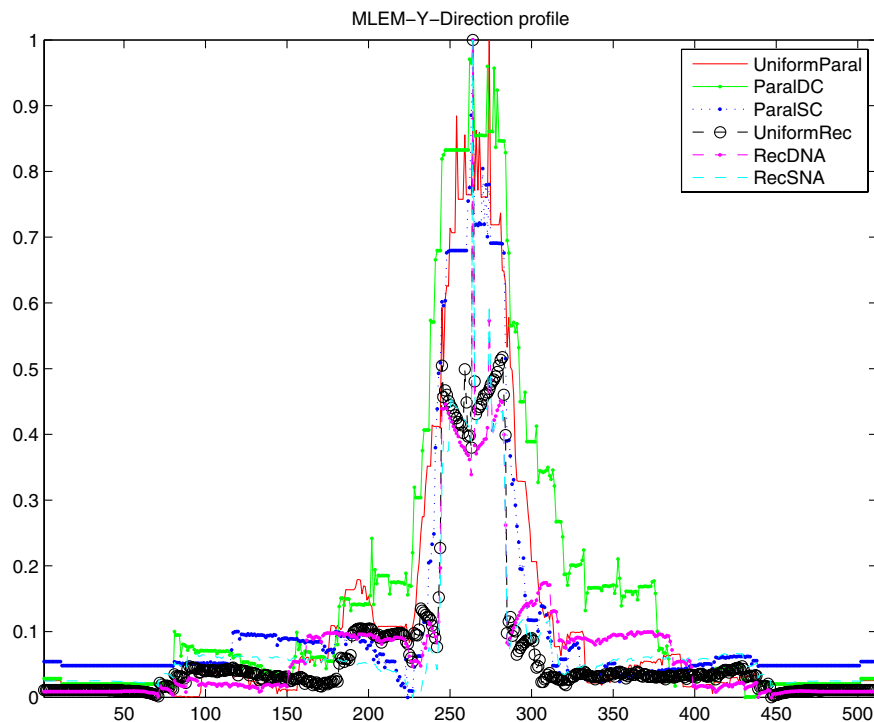

Fig. 19 Line profiles along the *Y* direction crossing the wire responses.

half maximum, one can see that the RecSNA shows the best z-resolution and all rectangle configurations outperform the parallel ones, which are consistent with the conclusion from the line profiles shown in Fig. 14. For instance, compared to UniformParal, the depth resolution from UniformRec is improved by almost one-fold.

Since the resolution is spatially dependent, we employ the average MTF over the nine impulse responses shown in Fig. 9. Average MTF is calculated by the sum of the subregional MTFs dividing the maximum. Figure 16 shows the normalized results. One can see parallel configurations show better X resolution than rectangle ones, that is because along X-direction, parallel configuration provides denser
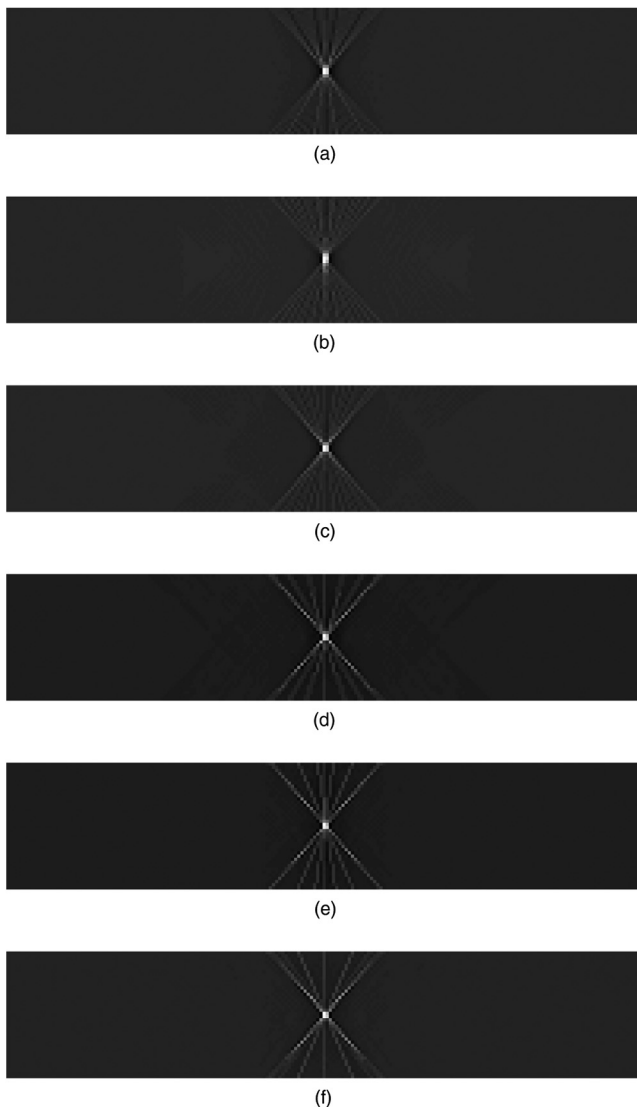

(a)

(b)

(c)

(d)

(e)

(f)

Fig. 20 The reconstructed results of wire signals on the $X - Z$ plane with the given image acquisition configurations. (a) The reconstructed result of wire signal on the $X - Z$ plane for UniformParal: less sharp response; (b) the reconstructed result of wire signal on the $X - Z$ plane for ParalDC: less sharp response; (c) the reconstructed result of wire signal on the $X - Z$ plane for ParalSC: sharper response; (d) the reconstructed result of wire signal on the $X - Z$ plane for UniformRec: sharper response; (e) the reconstructed result of wire signal on the $X - Z$ plane for RecDNA: sharper response; (f) the reconstructed result of wire signal on the $X - Z$ plane for RecSNA: sharper response.

samplings. For parallel shapes, uniform density exhibits slightly worse resolution than sparse center density, which is because the sparse center source produces best resolution at edge locations due to the dense sampling above these locations. Therefore, with respect to average MTF, ParalSC is slightly better than uniformParal.

3.2 Wire Response of the Six Source Distributions in the Tomosynthesis System

Figures 17(a)–17(f) show the reconstructed results of wire signal on transverse plane with the six source configuration. This plane is 30 mm away from the detector surface. Only the middle point on this wire is located on the plane. Other textures are out-of-plane artifacts. It is clear to see that in the rectangle configurations, the middle points of the wires are much sharper than those from the parallel configurations. Moreover, the out-of-plane textures within the rectangle shapes are suppressed better than those with the parallel shapes.

Figure 18 shows the line profiles crossing the middle point of the wires shown in Figs. 17(a)–17(f). The line profiles show consistent results presented in Fig. 12, which are that the rectangle configuration can suppress artifacts better and provide higher contrast.

Figure 19 draws the line profiles along the Y-direction intersected with the wire signal on the focus plane. This figure shows the capability to remove the out-of-plane blur. Along the line profile, only one point is the on-plane point of a wire, and others are artifacts shadowed from
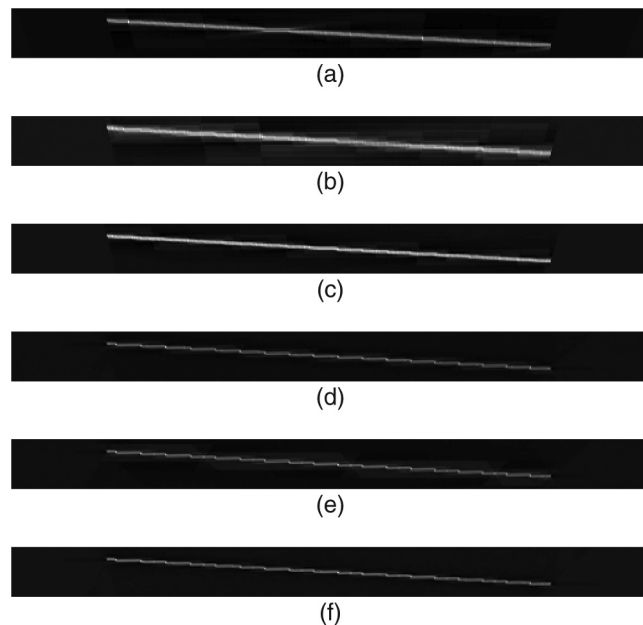

(a)

(b)

(c)

(d)

(e)

(f)

Fig. 21 The reconstructed results of wire signals on $Y - Z$ plane with the given source configurations. (a) The reconstructed result of wire signal on the $Y - Z$ plane for UniformParal: less sharp edge; (b) the reconstructed result of wire signal on the $Y - Z$ plane for ParalDC: less sharp edge; (c) the reconstructed result of wire signal on the $Y - Z$ plane for ParalSC: less sharp edge; (d) the reconstructed result of wire signal on the $Y - Z$ plane for UniformRec: sharp edge; (e) the reconstructed result of wire signal on the $Y - Z$ plane for RecDNA: sharper edge; (f) the reconstructed result of wire signal on the $Y - Z$ plane for RecSNA: sharper edge.
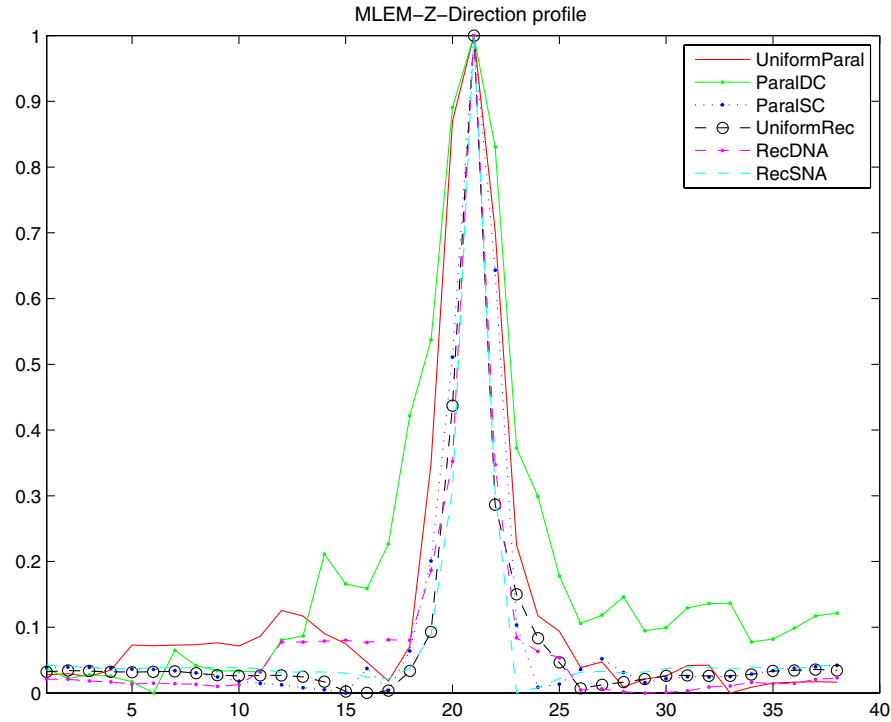
Fig. 22 Line profiles along the Z direction crossing the wire response.

other planes. Rectangle configurations effectively suppress the out-of-plane blur and turn out a better resolution in Y-direction, which is because the presence of sources along Y-direction can reduce the uncertainty along the same direction. For the parallel configurations, the ability to reduce out-of-plane of uniform configuration is better than that of ParalDC, but worse than that of ParalSC. The differences among rectangle configurations are not as obvious as those of parallel configurations.

Figures 20(a)–20(f) present the reconstructed results in X–Z plane. The signals show sharper edge along the vertical direction in rectangle configurations and ParalSC.
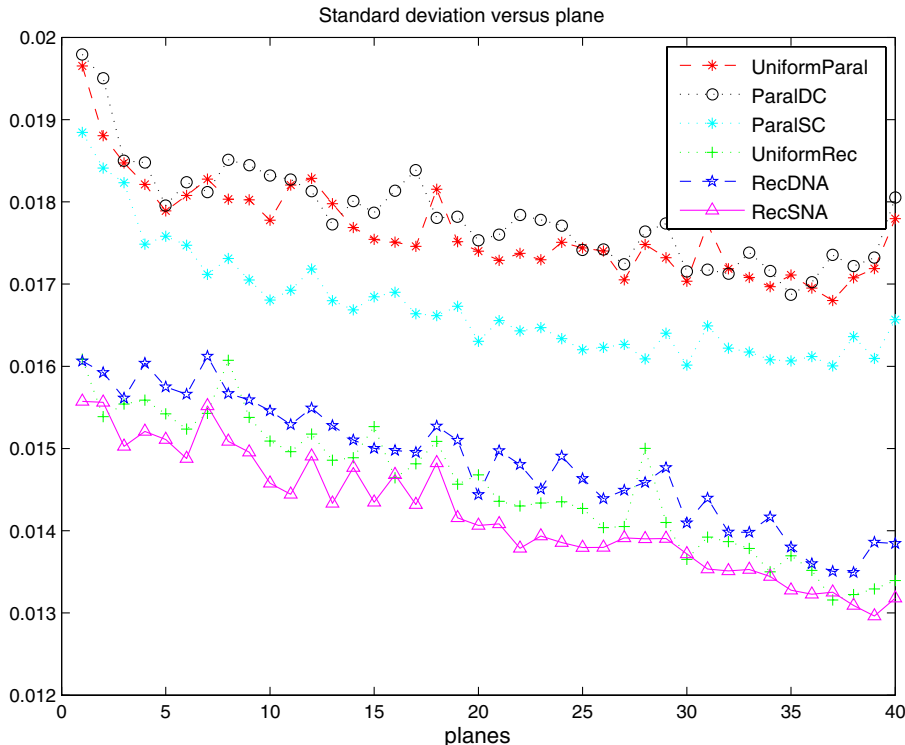

Fig. 23 Standard deviation for each reconstructed plane.

Figure 21(a)–21(f) shows the reconstructed results in Y–Z plane. In these results, the edge of the wire responses in the Y–Z plane is presented. It is obvious that the rectangle configuration provides much sharper edges and higher resolution than parallel configurations.

Figure 22 shows the line profiles along the Z-direction crossing the wire response shown in Fig. 21. As observed in Figs. 21(a)–21(f), rectangle configurations produce much higher depth resolution. For parallel configurations, the depth resolution of uniform configuration is better than that of ParalDC but worse than that of ParaSC. As to the rectangle configurations, the RecSNA provides a slightly better resolution than the other two, whereas both UniformRec and RecDNA yield similar results.

3.3 Noise Property of the Six Source Distributions in the Tomosynthesis System

Figure 23 reports the standard deviation on each reconstructed plane over all source configurations. In general, rectangle configuration outperforms parallel configuration in terms of noise suppression. For rectangle configurations, UniformRec produces less noise than RecDNA, but a slightly higher noise than RecSNA. As to parallel configurations, ParaSC shows obviously superior noise property to the others. ParalDC gives a similar result with UniformParal.

4 Conclusions

The CNT-based spatially distributed multibeam x-ray tubes applied in breast tomosynthesis enable the potentials to improve 3-D image qualities by a wide variety of flexible beam sources configurations. In this study, we investigated the sources distributed on a 2-D rectangle plane by computer simulations, and compared the results with a 1-D parallel configuration. Some preliminary results have been presented.

In most cases, rectangle shapes outperform parallel shapes by providing better Z-direction resolution, enhanced image contrast, reduced out-of-plane blur and artifacts on the edge and lower reconstruction noise. However, parallel configurations show better X-direction resolution due to their denser samplings along X-direction.

Considering uniform and nonuniform density for the parallel configurations, ParalSC provides more suppressed out-of-plane blur and a better depth resolution than the other two, whereas ParaDC demonstrates better X-Y resolution. For rectangle configurations, RecSNA yields the best depth resolution, however, for other aspects, the differences between various distributions are less obvious.

The benefits from the rectangle configuration may expand the application from early screening to imaging guide therapy. Further works need to be done to investigate more parameters for the rectangle configurations, such as total view angles, projection numbers, or slice-thickness, to optimize the tomosynthesis system with spatially distributed multibeam source to accommodate more applications.

References

1. J. T. Dobbins, III, "Tomosynthesis imaging: at a translational crossroads," *Med. Phys.* **36**(6), 1956–1967 (2009).
2. J. T. Dobbins, III and D. J. Godfrey, "Digital X-ray tomosynthesis: current state of the art and clinical potential," *Phys. Med. Biol.* **48**(19), 65–106 (2003).
3. Y. Chen, "Digital breast tomosynthesis (DBT)—a novel imaging technology to improve early breast cancer detection: implementation, comparison and optimization," Ph.D. Diss., Duke University (2007).
4. Y. Zhang et al., "A comparative study of limited-angle cone-beam reconstruction methods for breast tomosynthesis," *Med. Phys.* **33**(10), 3781–3795 (2006).
5. A. Smith"Design Considerations in Optimizing a Breast Tomosynthesis System," http://www.hologic.com/data/Design_Considerations_Optimizing_Breast_Tomo.pdf.
6. Y. Lu et al., "Effects of projection-view distributions on image quality of calcifications in digital breast tomosynthesis (DBT) reconstruction," *Proc. SPIE* **7622**, 76220D (2010).
7. I. Sechopoulos and C. Ghetti, "Optimization of the acquisition geometry in digital tomosynthesis of the breast," *Med. Phys.* **36**(4), 1199–1207 (2009).
8. T. Mertelmeier et al., "Optimization of tomosynthesis acquisition parameters: angular range and number of projections," *Lect. Notes Comput. Sci.* **5116**, 220–227 (2008).
9. A. S. Chawla et al., "A mathematical model platform for optimizing a multi-projection breast imaging system," *Med. Phys.* **35**(4), 1337–1345 (2008).
10. A. S. Chawla et al., "Optimized image acquisition for breast tomosynthesis in projection and reconstruction space," *Med. Phys.* **36**(11), 4859–4869 (2009).
11. X. Qian et al., "High resolution stationary digital breast tomosynthesis using distributed carbon nanotube x-ray source array," *Med. Phys.* **39**(4), 2090–2099 (2012).
12. X. Qian et al., "Design and characterization of a spatially distributed multibeam field emission x-ray source for stationary digital breast tomosynthesis," *Med. Phys.* **36**(10), 4389–4400 (2009).
13. A. Tucker, J. Lu, and O. Zhou, "Dependency of image quality on system configuration parameters in a stationary digital breast tomosynthesis," *Med. Phys.* **40**(3), 031917 (2013).
14. D. J. Godfrey, H. P. McAdams, and J. T. Dobbins III, "Optimization of the matrix inversion tomosynthesis (MITS) impulse response and modulation transfer function characteristics for chest imaging," *Med. Phys.* **33**(3), 665–667 (2006).
15. A. H. Andersen, "Algebraic reconstruction in CT from limited view," *IEEE Trans. Med. Imaging* **8**(1), 50–55 (1982).
16. A. H. Andersen and A. C. Kak, "Simultaneous algebraic reconstruction technique (SART): a superior implementation of the ART algorithm," *Ultrosonic Imaging* **6**(1), 740–753 (1996).
17. K. Lange and J. A. Fessler, "Globally convergent algorithms for maximum a posteriori transmission tomography," *IEEE Trans. Image Process.* **4**(10), 1430–1438 (1995).
18. K. Lange, M. Bahn, and R. Little, "A theoretical study of some maximum likelihood algorithms for emission and transmission tomography," *IEEE Trans. Med. Imaging* **6**(2), 106–114 (1987).
19. E. J. Candes, J. Romberg, and T. Tao, "Robust uncertainty principles: exact signal reconstruction from highly incomplete frequency information," *IEEE Trans. Inf. Theory* **52**(2), 486–509 (2006).
20. H. Turbell, "Cone beam reconstruction using filtered backprojection," Ph.D. Diss. Dep. Electr. Eng., Linkoping University (2001).
21. A. D. Pierro, "On the relation between the ISRA and the EM algorithm for positron emission tomography," *IEEE Trans. Med. Imaging* **12**(2), 328–333 (1993).
22. H. Erdogan and J. A. Fessler, "Monotonic algorithms for transmission tomography," *IEEE Trans. Med. Imaging* **18**(9), 801–814 (1999).
23. T. Wu et al., "Tomographic mammography using a limited number of low-dose cone-beam projection images," *Med. Phys.* **30**(3), 365–380 (2003).
24. S. Xu et al., "An application of pre-computed backprojection based penalized-likelihood (PPL) image reconstruction on stationary digital breast tomosynthesis," *Proc. SPIE* **8668**, 86680V (2013).
25. S. Xu, H. Schurz, and Y. Chen, "Parameter optimization of relaxed ordered subsets pre-computed back projection (BP) based penalized-likelihood (OS-PPL) reconstruction in limited-angle x-ray tomography," *J. Comput. Med. Imaging Graph. Artic. Press* **37**(4), 304–312 (2013).
26. S. Xu and Y. Chen, "A simulation based image reconstruction strategy with predictable image quality in limited-angle x-ray tomography," *Proc. SPIE* **8668**, 86685P (2013).
27. I. A. Elbakri and J. A. Fessler, "Statistical x-ray computed tomography image reconstruction with beam hardening correction," *Proc. SPIE. Medical Imaging: Image Processing* **4322**, 1–12 (2001).
28. I. A. Elbakri and J. A. Fessler, "Efficient and accurate likelihood for iterative image reconstruction in x-ray computed tomography," *Proc. SPIE* **5032**, 1839–1850 (2003).
29. B. R. Whiting, "Signal statistics in x-ray computed tomography," *Proc. SPIE* **4682**, 53–60 (2002).

Shiyu Xu is a PhD candidate in the electrical and computer engineering department, Southern Illinois University Carbondale, Illinois. His research interests include medical imaging, image reconstruction, and general image processing. Right now, he is a research intern of CT Systems & Algorithms, at GE Healthcare. His works are involving both model-based iterative reconstruction and advanced analytic reconstruction. He holds mathematics and electrical engineering MS and BS degree at Beijing University of aeronautics and astronautics.

Linlin Cong was a master's student in the electrical and computer engineering department, Southern Illinois University Carbondale, Illinois. Her research interests include image reconstruction and image system optimization. Right now, she is a PhD student in the BME program at University of Texas at San Antonio.

Jianping Lu is a professor of department of physics and astronomy curriculum in applied and materials science. His research focuses on physics of carbon nanotubes and applications of carbon nanotubes. He received his PhD degree in physics from the City University of New York in 1988 and was a research associate in the University of Chicago and the University of Illinois at Urban Champaign.

Otto Zhou is David Godschalk distinguished professor for physics and materials sciences at the University of North Carolina. The research in his lab focuses on developing advanced instrumentations for diagnostic medical imaging and radiation therapy utilizing the carbon nanotube based field emission x-ray source technology pioneered. He received his PhD degree from the University of Pennsylvania and worked as a researcher at the Bell Labs and NEC.

Yueh Z. Lee is an assistant professor of radiology and physics. He received his medical degree from UNC where he also obtained a PhD in biomedical engineering. He completed his neuroradiology training also at UNC. His areas of interest are brain tumors and new imaging techniques. He serves as a "translational" scientist and clinical neuroradiologist and is serving a key role in the development of the carbon nanotube CT scanner.

Ying Chen obtained her PhD from Duke University. She is an associate professor in the Electrical and Computer Engineering Department at Southern Illinois University, Carbondale, Illinois. She worked in Duke Advanced Imaging Laboratories, for theoretical and experimental studies of image reconstruction, image quality, and image analysis for digital tomosynthesis imaging. She also holds an MS degree in instrumentation (electrical engineering). Her current research focuses on medical imaging, image quality, computer vision, image processing, and analysis.